JACS
JOURNAL OF THE AMERICAN CHEMICAL SOCIETY
pubs.acs.org/JACS
Article

Regulating Catalytic Properties and Thermal Stability of Pt and PtCo Intermetallic Fuel-Cell Catalysts via Strong Coupling Effects between Single-Metal Site-Rich Carbon and Pt

Yachao Zeng,[¶] Jiashun Liang,[¶] Chenzhao Li,[¶] Zhi Qiao, Boyang Li, Sooyeon Hwang, Nancy N. Kariuki, Chun-Wai Chang, Maoyu Wang, Mason Lyons, Sungsik Lee, Zhenxing Feng, Guofeng Wang, Jian Xie,* David A. Cullen, Deborah J. Myers,* and Gang Wu*

Cite This: *J. Am. Chem. Soc.* 2023, 145, 17643−17655

Read Online

ACCESS | Metrics & More | Article Recommendations | Supporting Information

ABSTRACT: Developing low platinum-group-metal (PGM) catalysts for the oxygen reduction reaction (ORR) in proton-exchange membrane fuel cells (PEMFCs) for heavy-duty vehicles (HDVs) remains a great challenge due to the highly demanded power density and long-term durability. This work explores the possible synergistic effect between single Mn site-rich carbon (Mn_{SA}-NC) and Pt nanoparticles, aiming to improve intrinsic activity and stability of PGM catalysts. Density functional theory (DFT) calculations predicted a strong coupling effect between Pt and MnN_4 sites in the carbon support, strengthening their interactions to immobilize Pt nanoparticles during the ORR. The adjacent MnN_4 sites weaken oxygen adsorption at Pt to enhance intrinsic activity. Well-dispersed Pt (2.1 nm) and ordered $L1_2$-Pt_3Co nanoparticles (3.3 nm) were retained on the Mn_{SA}-NC support after indispensable high-temperature annealing up to 800 °C, suggesting enhanced thermal stability. Both PGM catalysts were thoroughly studied in membrane electrode assemblies (MEAs), showing compelling performance and durability. The Pt@Mn_{SA}-NC catalyst achieved a mass activity (MA) of 0.63 A mg_{Pt}^{-1} at 0.9 $V_{iR\text{-free}}$ and maintained 78% of its initial performance after a 30,000-cycle accelerated stress test (AST). The $L1_2$-Pt_3Co@Mn_{SA}-NC catalyst accomplished a much higher MA of 0.91 A mg_{Pt}^{-1} and a current density of 1.63 A cm^{-2} at 0.7 V under traditional light-duty vehicle (LDV) H_2−air conditions (150 kPa_{abs} and 0.10 mg_{Pt} cm^{-2}). Furthermore, the same catalyst in an HDV MEA (250 kPa_{abs} and 0.20 mg_{Pt} cm^{-2}) delivered 1.75 A cm^{-2} at 0.7 V, only losing 18% performance after 90,000 cycles of the AST, demonstrating great potential to meet the DOE targets.

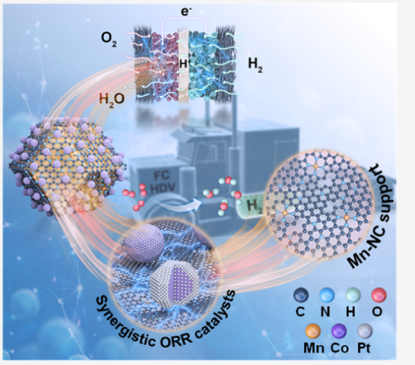

1. INTRODUCTION

Proton-exchange membrane fuel cells (PEMFCs) have been recognized as a critical alternative power source to the combustion of fossil fuels, enabling the transition to a carbon-neutral economy, given their capability to convert clean hydrogen to electricity with high efficiencies and high energy density.[1] Recently, their heavy-duty vehicle (HDV) applications have attracted considerable attention due to hydrogen's high gravimetric energy density, high energy efficiency, fast refueling, zero-emission, and less complex infrastructures for hydrogen refueling.[2] However, due to the significantly longer required lifetime of up to one million miles of operation, HDV applications impose stringent efficiency and long-term durability.[3,4] Generally, the performance and lifetime of PEMFCs are primarily governed by the activity and stability of the cathode electrocatalysts due to the sluggish kinetics of the oxygen reduction reaction (ORR).[5] It is essential to develop active and stable electrocatalysts through novel material design to meet the challenging power and cost targets for HDV applications (i.e., 2.5 kW per g_{PGM} power, 1.07 Acm^{-2} current density at 0.7 V after a 25,000 h equivalent accelerated durability test—AST, and $80 per kW_{net}).[3]

The conventional electrocatalysts for the ORR are carbon-supported platinum-group-metal (PGM) nanoparticles (NPs), such as Pt/C. Unfortunately, current Pt/C catalysts suffer from insufficient activity and stability.[6,7] Alloying Pt with other 3d transition metals (M), such as Co or Ni, can dramatically increase the ORR activity.[8,9] However, under the harsh working conditions of PEMFCs, the transition metals in Pt−M alloys are prone to dissolution, leading to a decrease in the catalytic activity. The leached transition metal ions also hinder proton conductivity and oxygen diffusion within ionomer layers, causing significant performance degradation.[8,10]

Received: March 30, 2023
Published: August 4, 2023

https://doi.org/10.1021/jacs.3c03345
J. Am. Chem. Soc. 2023, 145, 17643−17655

Alternatively, Pt−M alloys can be converted to ordered Pt−M intermetallics via thermal annealing, where Pt and M atoms arrange periodically within the crystallites. Such ordered structures and strong Pt−M bonds can effectively restrain the dissolution of M, leading to a much-enhanced stability for the ORR.[10] Therefore, ordered Pt−M intermetallics are considered one of the most promising ORR cathode catalysts.[10−13] Nevertheless, one key challenge for Pt−M intermetallics is the control of the NP sizes. During the indispensable high-temperature annealing for phase transition, the NPs are thermodynamically unstable and tend to move/aggregate into large NPs due to the weak metal−support interaction.[14,15] Large particles are unfavorable for high-performing PEMFC due to reduced electrochemically active surface areas (ECSAs). Therefore, effective strategies to mitigate particle aggregation with enhanced thermal stability during high-temperature annealing are essential to obtain well-dispersed and highly ordered intermetallic structures.

The catalyst support is one essential component of cathode catalysts, providing adequate electrical conductivity and dispersing fine PGM NPs to achieve sufficient ECSAs. Most Pt-based NPs are supported on commercial carbon powder (Ketjen black, Vulcan XC-72, etc.). However, PGM NPs on these commercial carbon materials would migrate, agglomerate, or detach under dynamic fuel-cell operating conditions due to insufficient interactions, resulting in severe loss of ECSA and significant performance degradation.[16−20] Carbon corrosion during vehicle start-up or shut-down exacerbates the weakening of the Pt−carbon interaction, further driving Pt NP detachment from the support and ECSA loss.[21] Meanwhile, carbon support degradation can also lead to catalyst layer thinning and pore structure collapse, undermining the electrode's mass and electron transport properties.[22] Currently, alternative oxide supports still exhibit insufficient electrical conductivity and/or a low surface area along with poor Pt NP dispersion.[18,23] Therefore, rational design and engineering of a carbon support to preserve the particle size, boost chemical/electrochemical stability, and strengthen the catalyst−support interaction are critical to achieving enhanced activity and stability of low-PGM catalysts for HDV applications.

As the most promising PGM-free catalysts, atomically dispersed metal sites coordinated with nitrogen and embedded in carbon (M_{SA}−N−C, M = Fe, Co, Mn, etc.),[24−30] i.e., single-atom catalysts (SACs), have emerged as a promising support for Pt or Pt alloy catalysts.[18,31−33] Featuring a hierarchical pore structure, high surface area, adjustable particle sizes, and abundant heterogeneous dopants, these M_{SA}−N−C carbon materials likely provide a remarkable support effect for PGM catalysts. The M_{SA}−N−C support could also provide an electronic metal−support interaction (EMSI) between Pt and atomically dispersed MN_4 sites, improving catalyst performance and durability and reducing Pt usage.[31,32,34,35] For example, Fe−N−C has been employed to support Pt and PtM NPs, and these synergistic catalysts demonstrated encouraging performance in PEMFCs.[31,35,36] However, Fe-based species likely catalyze Fenton reactions to generate reactive oxygenated species (ROS), especially during long-term operation with H_2O_2 accumulation. The resultant ROS degrades the membrane and ionomer in the catalyst layer and poses a significant risk to long-term stability for PEMFCs.[37] It is unclear which SAC is the optimal catalyst support, and the synergistic effect underlying single-atom-catalyst-supported Pt remains unclear. The design principle of the synergistic catalysts must be elucidated.

This work reports synergistic Pt or ordered $L1_2$-Pt_3Co NP catalysts on an atomically dispersed MnN_4 site-rich carbon support. Comprehensive experimental results and DFT calculations indicate that the MnN_4 site could induce a strong coupling effect between Pt clusters and the carbon support. The possible synergy could enhance the chemical binding between Pt clusters and the Mn−NC support, improving catalyst stability and weakening the adsorption strength of OH at Pt surfaces with enhanced intrinsic ORR activity. DFT calculations predict that among different SACs, MnN_4 is the optimal chemical dopant in carbon to strengthen the Pt−support interaction and enhance the ORR activity. In agreement with these theoretical predictions, ultrafine Pt and $L1_2$-Pt_3Co intermetallic NPs supported on Mn_{SA}-NC achieved compelling activity and stability, evidenced by rotating ring-disk electrode (RRDE) tests and comprehensive membrane electrode assembly (MEA) tests. In particular, the Pt@Mn_{SA}-NC-based MEA with a low loading of 0.1 mg_{Pt} cm^{-2} generated a significantly improved ORR mass activity (MA) of 0.63 A mg_{Pt}^{-1} at 0.9 $V_{iR\text{-free}}$ and retained 78% of the initial value after 30,000 voltage cycles for a catalyst accelerated stress test (AST). Also, the $L1_2$-Pt_3Co@Mn_{SA}-NC-based MEA with an identical Pt loading achieved an enhanced MA of 0.91 A mg_{Pt}^{-1}. The $L1_2$-Pt_3Co@Mn_{SA}-NC catalyst reached a power density of 1.14 W cm^{-2} at 0.7 V (1.63 A cm^{-2}), losing only 27% of this initial performance after the AST cycling. Furthermore, under HDV conditions (0.2 mg_{Pt} cm^{-2} and 250 kPa_{abs}), the $L1_2$-Pt_3Co@Mn_{SA}-NC catalyst delivered a record current density of 1.75 A cm^{-2} at 0.7 V and promising long-term durability (18% loss of current density and 37% loss in the MA after a 90,000-cycle AST).

Significantly mitigated Pt and Pt−Co NP agglomeration is observed in post-mortem analysis of the MEAs (under LDV conditions), attesting to the high stability of the Pt@Mn_{SA}-NC catalyst during the ORR under fuel-cell environments. The synergistic effect between atomically dispersed MnN_4 site-rich carbon and PGM NPs elucidated in this work may shed light on the design of highly efficient catalysts for PEMFCs regarding the newly emerging HDV applications.

2. RESULTS AND DISCUSSION

2.1. Synergistic Effects between Pt and the M_{SA}-N−C Support. A series of synergistic catalysts, consisting of the Pt NPs and carbon-based single-atom catalyst (SAC) support, is studied for the ORR. First, the Ni-, Co-, and Mn-based SAC carbon support (M_{SA}-NC) was developed through multiple effective methods based on zeolitic imidazolate frameworks (ZIFs-8).[38] The particle size of the single-metal site-rich carbon support was deliberately controlled to be ca. 100 nm to ensure a similar mass transport in electrodes for electrochemical characterization.

Four types of carbon supports, including three SACs and one carbonized ZIF-8 (ZIF-NC), were characterized using X-ray diffraction (XRD) patterns, Raman spectroscopy, and Brunauer−Emmett−Teller (BET) analysis. According to XRD patterns, no metallic phases are detected in the support (Figure S1a), indicating that Mn, Ni, and Co species are likely atomically dispersed. In Raman spectra, the D band (I_D) at ∼1350 cm^{-1} and the G band (I_G) at ∼1600 cm^{-1} reflect the disordered sp^3 carbon atoms at the edge and the crystallization of sp^2-hybridized carbon atoms in an ideal graphene layer,

https://doi.org/10.1021/jacs.3c03345
J. Am. Chem. Soc. 2023, 145, 17643−17655

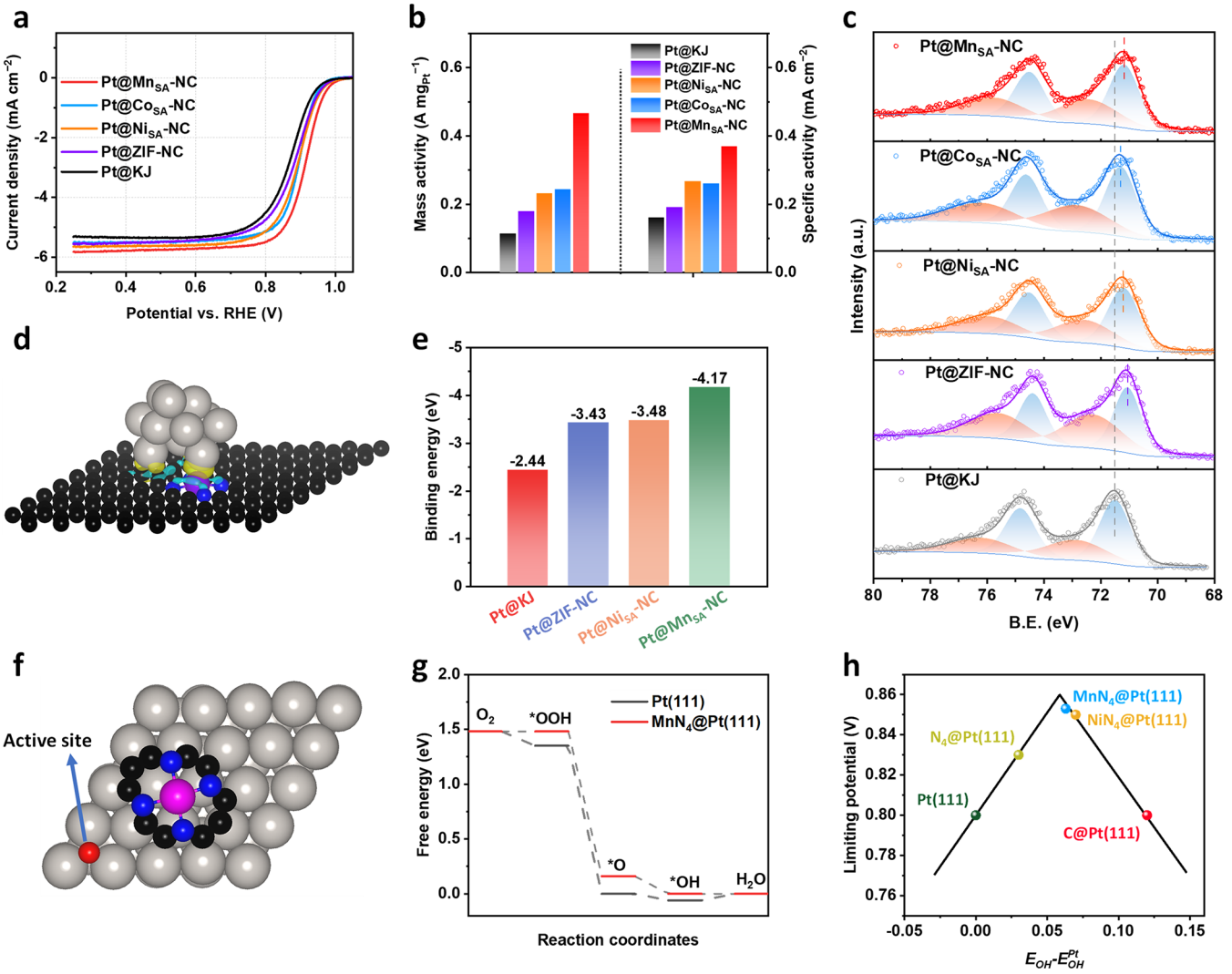

Figure 1. (a) ORR activities of the prepared catalysts in an O_2-saturated 0.1 M $HClO_4$. (b) Comparison of mass-specific and active surface area-specific activities of the Pt catalysts at 0.9 V by using different single-atom-rich carbon supports. (c) Pt 4f XPS of the Pt catalysts supported on ZIF-NC and SACs, in which Pt@Ketjen Black and Pt@ZIF-NC served as the baseline. (d) Optimized atomistic structure of a 13-atom Pt_{13} cluster adsorbed on an MnN_4 moiety embedded in a graphene layer. (e) Binding energy between a Pt_{13} cluster and different supports. (f) Optimized atomistic structure of oxygen atom adsorption on the MnN_4@Pt(111) catalyst. In these figures, the black, blue, purple, red, white, and gray balls represent the C, N, Mn, O, H, and Pt atoms, respectively. (g) Calculated free energy evolution along the four-electron associative ORR pathway on MnN_4@Pt(111) and Pt(111) catalysts under an electrode potential of 0.86 V. (h) Volcano plot showing the ORR limiting potential as a function of the binding energy of OH on Pt(111) with various supports. The data to fit the volcano plot (the two black lines) are from the reference.[5]

respectively.[39] The I_G/I_D values of the obtained support are ~1.15, suggesting a similar and relatively high degree of graphitization (Figure S1b). According to BET results, Mn_{SA}-NC shows the highest surface area (1085.3 $m^2\ g^{-1}$) among the studied support (Figure S2 and Table S1). Also, ZIF-NC and Mn_{SA}-NC supports have considerable microporosity, providing abundant anchoring sites for Pt NPs. In addition, Mn_{SA}-NC contains significant mesoporosity (Figure S2c), favoring mass transport and ionomer dispersion within electrodes.

Pt NPs with a favorable particle size (~3 nm) were deposited on various SAC supports using an impregnation method.[31] Briefly, Pt salt (H_2PtCl_6) was mixed with a carbon support via sonication, followed by freeze-drying. The obtained powder was subjected to thermal annealing under forming gas (10% H_2/Ar) at 600 °C to obtain Pt@M_{SA}-NC catalysts. The Pt@M_{SA}-NC (M = Mn, Co, Ni) catalysts were evaluated using RRDE to determine their intrinsic activity and stability. Commercial Ketjen black (KJ) carbon was employed as a comparison. As shown in Figure S3a,b, the Pt@Mn_{SA}-NC catalyst achieves an impressive ECSA of 125.8 $m^2\ g_{Pt}^{-1}$, which could be ascribed to the high BET surface area and abundant microporosity of the Mn_{SA}-NC support. Meanwhile, all Pt@M_{SA}-NC catalysts exhibit an ORR activity higher than that of Pt on KJ carbon. In particular, Pt@Mn_{SA}-NC generated a higher specific activity (SA) of 0.37 mA cm_{Pt}^{-2} at 0.9 V_{RHE}, suggesting enhanced intrinsic activity (Figure 1a,b). The stabilities of the Pt@M_{SA}-NC and Pt@KJ catalysts were screened by potential cycling (0.6−0.95 V) at 60 °C in aqueous acidic electrolytes. As shown in Figure S4, the Pt@Mn_{SA}-NC catalyst retains a high ECSA of 98.5 $m^2\ g_{Pt}^{-1}$, with only a 21% loss after 10,000 cycles. However, the ECSA loss was 69% for the Pt@KJ catalyst due to the weak Pt−support interaction, similar to previous reports.[15,40] Furthermore, the ORR half-wave potential ($E_{1/2}$) loss of the Pt@Mn_{SA}-NC catalyst is only 1 mV after the AST, much lower than that of Pt supported on KJ carbon. The activity and stability results from

https://doi.org/10.1021/jacs.3c03345
J. Am. Chem. Soc. 2023, 145, 17643−17655

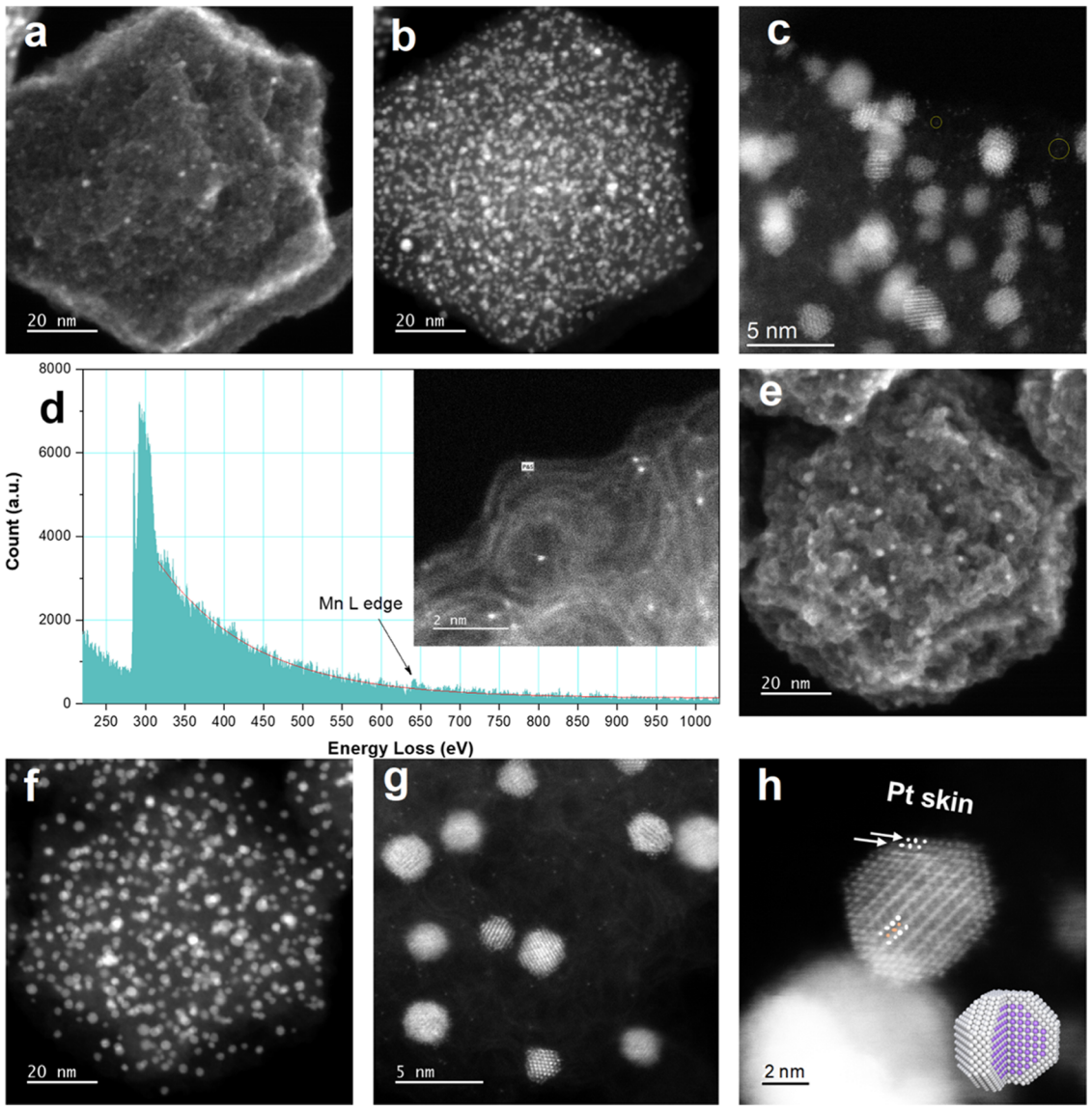

Figure 2. (a) Secondary electron (SE) microscopy and (b, c) HAADF-STEM images of Pt@Mn_{SA}-NC. (d) Atomic-resolution EELS result of Pt@Mn_{SA}-NC, showing the presence of Mn sites. Low magnified SE (e), HAADF-STEM images (f), and atomic-resolution (g, h) HAADF-STEM images of $L1_2$-Pt_3Co@Mn_{SA}-NC. Insets in panel (h) are the modeled nanoparticle with an $L1_2$ structure.

RDE further indicate that Mn_{SA}-NC carbon is superior in intrinsic activity and stability to the other single-metal site carbons explored in this work.

Figure 1c shows the X-ray photoelectron spectra (XPS) of Pt NPs on different types of M_{SA}-N−C support. The peaks with binding energies of approximately 71.5 and 74.5 eV can be correspondingly assigned to the $4f_{7/2}$ and $4f_{5/2}$ orbitals of metallic Pt, respectively.[41,42] Compared with the KJ carbon-supported Pt catalyst, notable negative shifts of the Pt 4f binding energy are observed for all M_{SA}-NC (M = Ni, Co, Mn)-supported catalysts, suggesting a strengthened metal−support interaction.[31,43] Notably, the Pt@Mn_{SA}-NC catalyst exhibited the most significant negative shift of the Pt 4f peaks. The Mn−N_4 sites may either interact with Pt NPs or alter the electronic structure of the neighboring C/N atoms, strengthening their interaction with Pt NPs. Such interactions may be beneficial for anchoring Pt NPs, thus improving stability during the ORR. Also, modifying the electronic structures of Pt could weaken the adsorption of O_2 and intermediate adsorption, thus enhancing intrinsic activity for the ORR.[18,44] We further correlate the ORR-specific activity (SA) with the binding energy shift of the Pt 4f peaks, presenting a well-defined volcano relationship (Figure S6). This suggests that the interaction between M_{SA}-NC and Pt, associated with modifying electronic structures, mainly depends on the nature of single-metal sites doped in carbon.

A series of Mn_{SA}-NC supports containing different Mn site contents were prepared via an adsorption approach with various amounts of Mn ion solution during the synthesis. Figure S7a shows that the ECSAs of these Pt catalysts were comparable (~120 m^2 g_{Pt}^{-1}). The Mn_{SA}-NC support with a high Mn content presents slightly increased ORR activity in the kinetic range (Figure S7b). Notably, enhanced catalyst stability was observed with an increasing Mn content in the carbon support (Figure S7c−f). These results suggest that the ORR activity and stability may correlate with single Mn site density in carbon support.

https://doi.org/10.1021/jacs.3c03345
J. Am. Chem. Soc. 2023, 145, 17643−17655

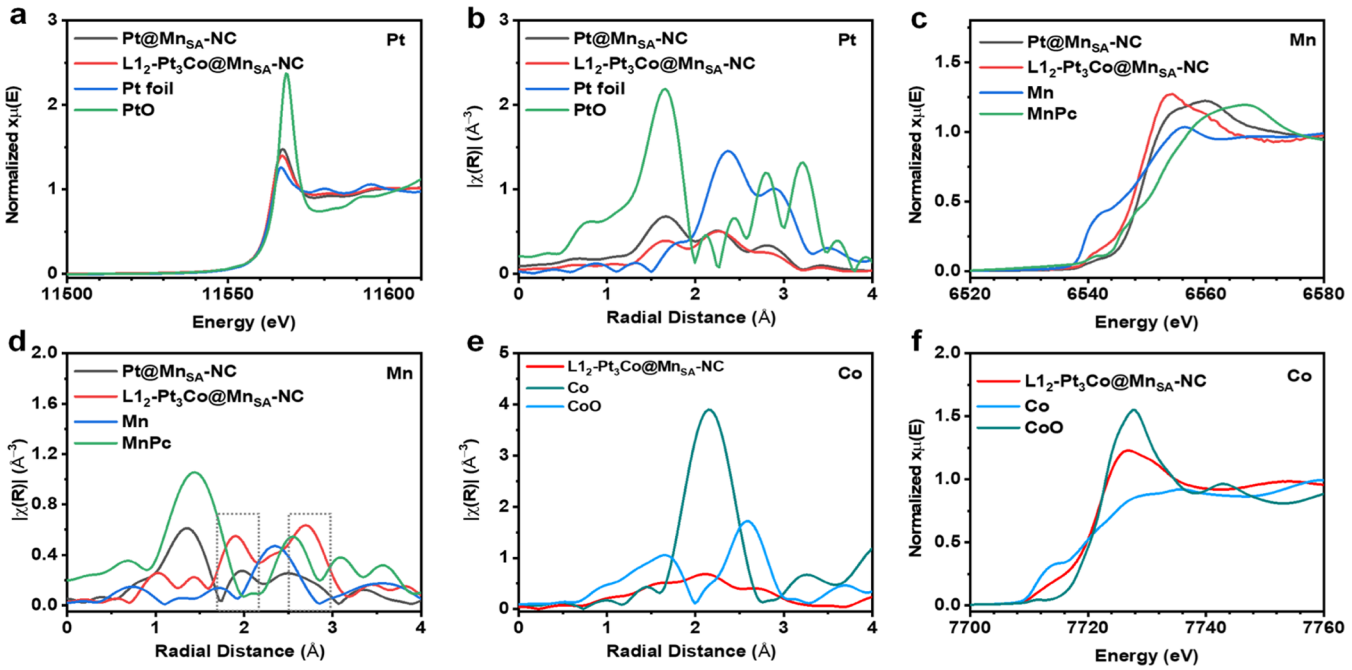

Figure 3. (a, c, f) XANES spectra of the Pt L_3-edge (a), Mn K-edge (c), and Co K-edge (f) for the Pt@Mn_{SA}-NC and $L1_2$-Pt_3Co@Mn_{SA}-NC catalysts. (b, d, e) Fourier-transformed EXAFS in the R-space of Pt (b), Mn (d), and the Co K-edge (e) for the Pt@Mn_{SA}-NC and $L1_2$-Pt_3Co@Mn_{SA}-NC catalysts.

Density functional theory (DFT) calculations were carried out to elucidate the possible synergy among single-metal sites, nitrogen dopants, and Pt clusters. We constructed four atomistic models consisting of a 13-atom cuboctahedra Pt_{13} cluster and a graphene layer with an MnN_4 moiety (Pt/MnN_4−C), a NiN_4 moiety (Pt/NiN_4−C), an N_4 moiety (Pt/N_4−C), and without dopants (Pt/C). The optimized atomistic structures are shown in Figures 1d and S8. Charge transfer analysis reveals that the introduction of an MN_4 moiety can modulate the interfacial charge density, which may affect the interaction between Pt and the support. We calculated the binding energies of the Pt/MnN_4−C, Pt/NiN_4−C, Pt/N_4−C, and Pt/C systems to be −4.17, −3.48, −3.43, and −2.44 eV, respectively (Figure 1e). A more negative binding energy value indicates a stronger interaction between the carbon support and Pt cluster. Therefore, the metal-N moieties, especially MnN_4, in the carbon support could lead to stronger binding to Pt NPs. The strengthened catalyst−support interaction could stabilize the Pt clusters by inhibiting their migration, detachment, or agglomeration.[44] We hypothesize that the Pt/MnN_4−C system would lead to the best stability among the four catalysts during the ORR, in agreement with experimental results.

We also performed DFT calculations to examine how the carbon support would affect the ORR activity of the Pt sites. As shown in Figures 1f and S9, we constructed four atomistic models consisting of a graphene plane with MnN_4, NiN_4, N_4 moieties, or no dopant and integrated them with a Pt(111) plane, respectively. These were denoted as MnN_4@Pt(111), NiN_4@Pt(111), N_4@Pt(111), and C@Pt(111). We first calculated the binding energy of OH (denoted as E_{OH}), a general descriptor, to evaluate the ORR activity. Introducing N_4 and MN_4 moieties can significantly reduce the E_{OH} (Figure S10), altering the rate-determining step (RDS) and improving intrinsic activity. The computational hydrogen electrode[45] (CHE) method was implemented to predict the free energy evolution along the four-electron associative ORR pathway on these model catalysts (Figures 1g and S11). The resulting free energy diagrams indicate that the introduction of the MN_4 moiety shifts the RDS from the desorption of *OH to the adsorption of *OOH.[5] Meanwhile, the limiting potentials, defined as the highest potential to allow each ORR elementary step to become exothermic, were calculated to be 0.80 V on Pt(111), 0.86 V on MnN_4@Pt(111), 0.85 V on NiN_4@Pt(111), 0.83 V on N_4@Pt(111), and 0.80 V on C@Pt(111). Moreover, we further correlated the calculated E_{OH} and the limiting potential, showing a well-defined volcano plot. MnN_4@Pt(111) is close to the apex (Figure 1h), suggesting that the MnN_4 moiety reduces E_{OH} to an optimal value and thus represents the most active catalyst among the studied systems. Therefore, the Mn_{SA}-NC support is desirable for Pt and PtCo catalysts with enhanced activity and stability.

2.2. Catalyst Structures. The morphologies and compositions of Pt@Mn_{SA}-NC and $L1_2$-Pt_3Co@Mn_{SA}-NC were comprehensively investigated using electron microscopy techniques (Figure 2). Mn_{SA}-NC carbon presents a highly concaved surface (Figure 2a), leading to high BET surface areas and favorable mass transport.[46] The particle size of Mn_{SA}-NC carbon ranges from 80 to 100 nm (Figure S12a), optimal for the mass transport and ionomer dispersion in catalyst layers based on previous studies.[47,48] High-resolution high-angle annular dark-field scanning transmission electron microscope (HAADF-STEM) images further reveal that Mn_{SA}-NC carbon has a highly porous structure with crumpled graphitic carbon layers on the surface (Figure S13a,b). Atomically dispersed sites with substantial density can be easily found in the Mn_{SA}-NC support (Figure S13d). Electron energy loss spectroscopy (EELS) analysis at atomic resolution further verifies single Mn sites in Mn_{SA}-NC (Figure S13e).

Ultrafine Pt NPs, with a mean diameter of 2.1 nm, are distributed uniformly on the surface and inside of the Mn_{SA}-NC carbon particles (Figure 2a,b). The concave morphology

https://doi.org/10.1021/jacs.3c03345
J. Am. Chem. Soc. 2023, 145, 17643−17655

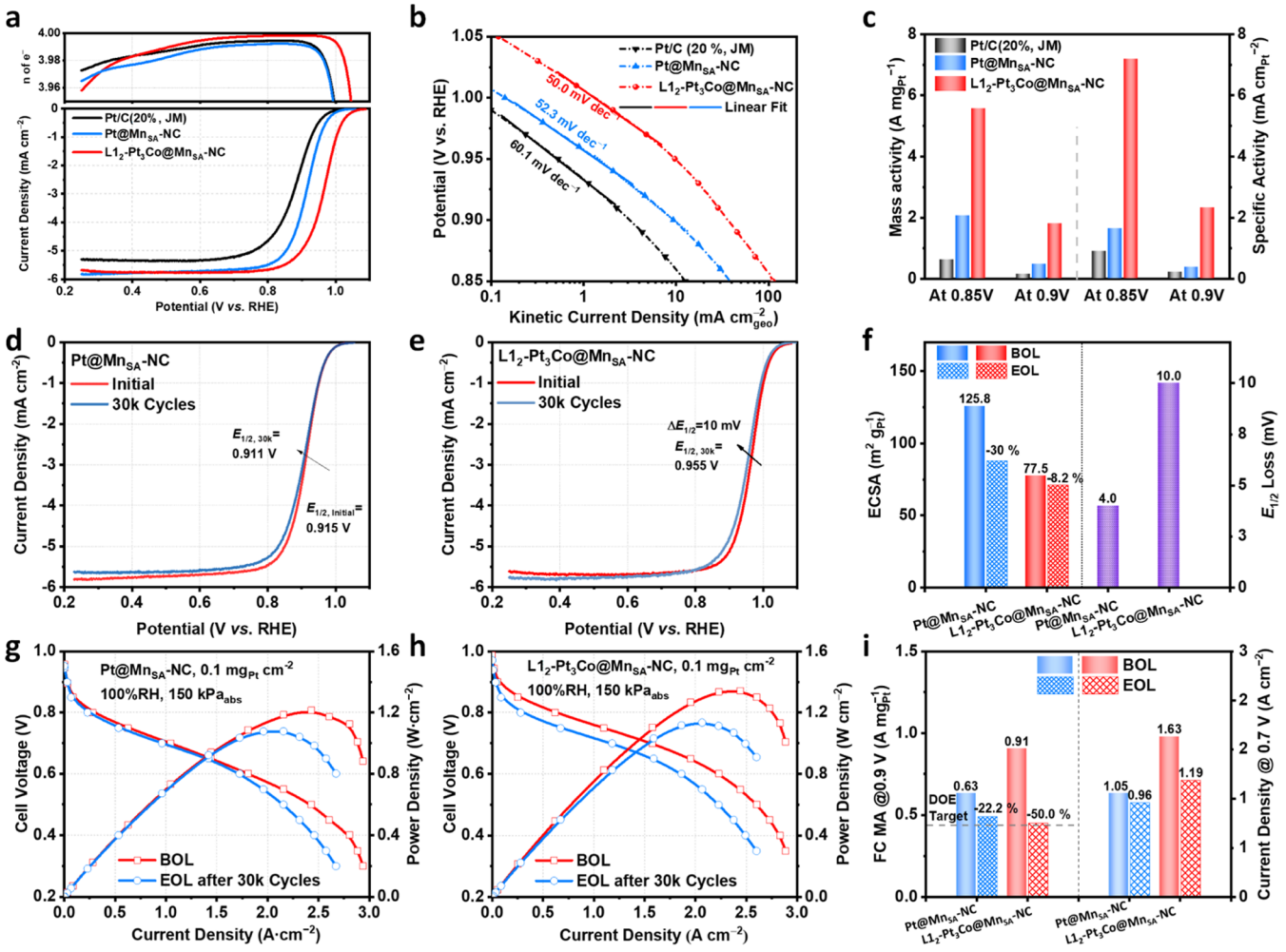

Figure 4. (a) ORR activities and selectivities of the prepared catalysts in an O_2-saturated 0.1 M $HClO_4$. (b) Comparison of the Tafel slopes of the prepared catalysts derived from Koutecky–Levich equations. (c) Comparison of mass-specific and active surface area-specific activities of the Pt catalysts with commercial Pt/C reference. (d, e) ORR activities of Pt@Mn_{SA}-NC (d) and $L1_2$-Pt_3Co@Mn_{SA}-NC (e) catalysts before and after the AST at 60 °C. (f) Comparison of the loss in the ECSA and $E_{1/2}$ before and after the AST. (g, h) BOL and EOL single-cell MEA performance during the AST of Pt@Mn_{SA}-NC (g) and Pt_3Co@Mn_{SA}-NC (h) cathodes under light-duty vehicle (LDV) conditions. Pt loading in the cathode: 0.1 mg_{Pt} cm^{-2}, back pressure: 150 kPa_{abs}, 80 °C, 100% RH, and H_2/air. (i) Mass activity (MA@0.9 $V_{iR\text{-free}}$, O_2) and current density (air) at 0.7 V of Pt@Mn_{SA}-NC and $L1_2$-Pt_3Co@Mn_{SA}-NC cathodes before and after 30,000 cycles of the AST under LDV conditions.

and inner pore structure can physically immobilize the Pt NPs and mitigate the migration and coalescence during the ORR. The HAADF-STEM image shows the atomically dispersed metal site around Pt NPs (Figure 2c). The coupled EELS analysis confirms that they are single Mn sites (Figure 2d). As predicted by DFT calculations, the proximity of Pt NPs and atomically dispersed Mn sites may induce synergistic ORR by tailoring the electronic configuration of Pt and modifying the adsorption of O_2 and *OH.

Likewise, ordered $L1_2$-Pt_3Co NPs were well dispersed on the Mn_{SA}-NC carbon support via a similar synthesis process, as evidenced by the corresponding HAADF-STEM images (Figures 2e–g and S14). The average particle size remains at 3.3 nm even after annealing at 800 °C, a critical step to form ordered intermetallic structures (Figure S14f). HAADF-STEM images and EELS analysis also show the possible presence of MnN_4 sites surrounding PtCo NPs (Figure S14g,h). STEM images indicate the periodic arrangement of bright (Pt) and dark (Co) atoms within a PtCo NP (Figure 2h). The corresponding fast Fourier transform (FFT) result shows superlattice spots, proving an ordered structure (Figure S14i). In addition, a compact Pt skin coating with 2–3 atomic layers on the PtCo intermetallic core appears due to acidic leaching and reductive thermal annealing treatments during the synthesis (Figure 2h). In addition, STEM-EDS elemental mappings indicate that Pt and Co elements are uniformly distributed within the nanoparticles and that the Pt/Co ratio is about 73/27, close to 3:1 in the Pt_3Co intermetallic structure (Figure S15).

The crystal structure of the $L1_2$-Pt_3Co@Mn_{SA}-NC catalyst was further studied by using XRD patterns. As shown in Figure S16, the as-prepared $L1_2$-Pt_3Co NP catalysts exhibited a slight shift to higher 2θ values for the diffraction peaks due to the partial replacement of the Pt atoms (radius: 1.39 Å) with smaller Co atoms (radius: 1.26 Å) inducing compression in the lattice. The diffraction peaks can be indexed to the typical structure of the $L1_2$-Pt_3Co intermetallic (JCPDS No. 96-152-4399), suggesting the formation of ordered $L1_2$-Pt_3Co, in good agreement with HAADF-STEM images. The ordering degree of $L1_2$-Pt_3Co@Mn_{SA}-NC, further calculated from the XRD data, was 61.1% (Figure S16).[10,11]

https://doi.org/10.1021/jacs.3c03345
J. Am. Chem. Soc. 2023, 145, 17643–17655

The oxidation state of metal elements and their electronic structures were further characterized using X-ray absorption spectroscopy (XAS).[49,50] The similar X-ray absorption near edge structure (XANES) of Pt in Pt@Mn_{SA}-NC and $L1_2$-Pt_3Co@Mn_{SA}-NC catalysts (Figure 3a) suggests their nearly identical oxidation states and *d*-band electron density. The oxidation states of Pt in both samples are approximately zero as the white line intensity, edge energy, and shapes of the XANES region are similar to metallic Pt. The extended X-ray absorption fine structure (EXAFS) analyses (Figure 3b) also indicate that Pt in Pt@Mn_{SA}-NC and $L1_2$-Pt_3Co@Mn_{SA}-NC shows scattering peaks at ∼2.3 Å attributed to Pt−Pt bonds. Compared to Pt foil, the Pt−Pt bond length is shortened due to the strain effect, which could benefit the ORR. Notably, the scattering peak at ∼1.6 Å can be attributed to Pt−O/N bonds, suggesting the possible interaction between Pt-based NPs and the Mn_{SA}-NC support or a trace amount of Pt oxides. The possible Pt−N bonding and the apparent negative shifts in the Pt 4f binding energy for all M_{SA}-NC (M = Ni, Co, Mn) in the XPS results further confirm the strengthened Pt−support interaction.

Additional XAS characterization at the Mn and Co K-edges of these catalysts was performed. As shown in Figure 3c, the Mn K-edge position in Pt@Mn_{SA}-NC is closer to that in MnPc, but with a slightly higher oxidation state than Mn in $L1_2$-Pt_3Co@Mn_{SA}-NC. A comparable intensity of the pre-edge 1s → 3d transition peak in Mn_{SA}-NC and MnPc suggests D_{4h} centrosymmetry of Mn, providing evidence for the existence of the square-planar Mn−N_4 configuration. No metallic Mn−Mn scattering paths are found in the Fourier transforms of the Mn K-edge EXAFS for the two PGM catalysts (Figure 3d). Specifically, the Pt@Mn_{SA}-NC catalyst shows a peak at 1.4 Å, which aligns with the Mn−N scattering path in MnPc, supporting the atomically dispersed and nitrogen-coordinated MnN_4 structures. Scattering paths at ∼2 and ∼2.5 Å were also found for both catalysts, possibly attributed to the interaction of Pt and Pt_3Co with Mn in the support.

This unique Pt and support interaction differs from the Pt and Co interactions in Pt_3Co nanoparticles. The weak metallic Pt−Co at ∼4 Å, which aligns with the similar Co−Co scattering path in the Co metal reference, was identified only in Co EXAFS of the $L1_2$-Pt_3Co@Mn_{SA}-NC catalyst (Figure 3e). The XANES in Figure 3f shows that, for the $L1_2$-Pt_3Co@Mn_{SA}-NC catalyst, the oxidation state of Co is between +2 and 0 when comparing the edge energy to that of the CoO and Co references, likely due to the alloying of Co with Pt in Pt_3Co. Overall, the XAS results unambiguously support the strong couple or interaction between Pt (or PtCo) and the unique Mn_{SA}-NC support.

2.3. ORR Activity and Stability. The activity and stability of Pt@Mn_{SA}-NC and $L1_2$-Pt_3Co@Mn_{SA}-NC catalysts were studied by using RRDE and compared to a Pt/C reference. The ECSAs of these catalysts are evaluated by electrochemical oxidation of monolayers of H atoms adsorb on Pt (Figure S17a). The Pt@Mn_{SA}-NC catalyst shows a notable $E_{1/2}$ of 0.915 V and an ECSA of 125.8 $m^2 g_{Pt}^{-1}$. Although high-temperature annealing was applied during the synthesis of the $L1_2$-Pt_3Co@Mn_{SA}-NC catalyst, a high ECSA (77.5 $m^2 g_{Pt}^{-1}$), comparable to that of commercial Pt/C (70.2 m^2 g_{Pt}^{-1}), was achieved (Figure S17b). This further verifies the advantages of the unique Mn_{SA}-NC support in suppressing Pt-based NP agglomeration during high-temperature annealing. Figure 4a shows a significant increase in $E_{1/2}$ to 0.965 V for the $L1_2$-Pt_3Co@Mn_{SA}-NC catalyst. The corresponding electron transfer numbers during the ORR are calculated at about four over an extensive potential range, as determined by using RRDE and Koutechy−Levich plots at different rotation speeds (Figures 4a and S17c−f).

In Figure 4b, the $L1_2$-Pt_3Co@Mn_{SA}-NC catalyst shows a higher kinetic current density than the Pt@Mn_{SA}-NC catalyst, especially at potentials above 0.9 V_{RHE}. In addition, the $L1_2$-Pt_3Co@Mn_{SA}-NC catalyst presents the lowest Tafel slope, with a value of 50.0 mV dec^{-1}. The mass activity (MA) and specific activity (SA) at 0.85 and 0.90 V_{RHE} for the studied catalysts are compared and summarized in Figure 4c. The $L1_2$-Pt_3Co@Mn_{SA}-NC catalyst presents the highest MA (1.8 A mg_{Pt}^{-1}) and SA (2.3 mA cm^{-2}) values, which could be ascribed to the reduced ORR activation energy due to strain and ligand effects of Pt_3Co intermetallic structures (Figure S18).[51,52]

The stability of Pt@Mn_{SA}-NC and $L1_2$-Pt_3Co@Mn_{SA}-NC catalysts was investigated by cycling between 0.60 and 0.95 V at 60 °C in a 0.1 M $HClO_4$ solution, a harsh condition close to the actual operating conditions of PEMFCs. As mentioned above, the Pt/C catalyst shows severe activity loss after only 10,000 cycles (Figures S4e and S5e). In contrast, the Pt@Mn_{SA}-NC catalyst exhibited significantly enhanced stability, with only 4 mV loss in $E_{1/2}$ and a high ECSA retention of 87.5 m^2 g_{Pt}^{-1} after 30,000 cycles (Figures 4d,f and S19a).

The stability improvement is likely due to the anchoring effect of the Mn_{SA}-NC support that hinders the aggregation of Pt NPs during the AST, as suggested by DFT calculations. In addition, the $L1_2$-Pt_3Co@Mn_{SA}-NC catalyst also showed encouraging durability, retaining 92% ECSA and losing only 10 mV in $E_{1/2}$ after 30,000 AST cycles (Figures 4e,f, and S19b).

2.4. MEA Performance and Stability under LDV Conditions. We further investigated various cathode catalysts, including commercial Pt/C, Pt@Mn_{SA}-NC, and $L1_2$-Pt_3Co@Mn_{SA}-NC catalysts in MEAs with a loading of 0.1 mg_{Pt} cm^{-2} and back pressure of 150 kPa (air) at the cathode (Figures 4g,4h and S20−S22). The commercial Pt/C cathode generated 0.65 A cm^{-2} at 0.7 V at BOL and lost 66% performance at EOL (Figure S20 and Table S2). In contrast, the Pt@Mn_{SA}-NC cathode achieved an impressive mass activity of 0.63 A mg_{Pt}^{-1} (O_2) at 0.9 $V_{iR\text{-free}}$, significantly higher than those of the commercial Pt/C catalysts with an identical Pt loading (Figure 4i). After 30,000 AST cycles, the performance loss in the kinetic range (above 0.7 V) was insignificant (Figure 4g). The MA of the Pt@Mn_{SA}-NC catalyst at EOL was 0.49 A mg_{Pt}^{-1}, corresponding to a 22% loss (Figure 4i). The current density at 0.7 V (air) was slightly decreased from 1.05 to 0.96 A cm^{-2}, indicating excellent stability in MEAs (Table S3), in good agreement with RDE tests in acidic electrolytes. The AST induced a slight loss in the peak power density, possibly caused by structural changes in the electrodes (Figure S22).

Similar to RDE results, the introduction of Co species improved the MEA performance significantly. The MA of the $L1_2$-Pt_3Co@Mn_{SA}-NC catalyst reached 0.91 A mg_{Pt}^{-1} (O_2) at 0.9 $V_{iR\text{-free}}$ (Figure 4i) and 1.63 A cm^{-2} at 0.7 V (air) under 75% relative humidity (RH) and back pressure of 150 kPa_{abs} conditions (Figure 4h and Table S4). The impact of RH% on the studied MEA performance is further illustrated in Figures S21 and S24. The $L1_2$-Pt_3Co@Mn_{SA}-NC-based MEA showed less dependence on RH% above 0.7 V. The cathode thicknesses of the Pt@Mn_{SA}-NC- and $L1_2$-Pt_3Co@Mn_{SA}-NC-based cathodes were reduced slightly after the AST. The

https://doi.org/10.1021/jacs.3c03345
J. Am. Chem. Soc. 2023, 145, 17643−17655

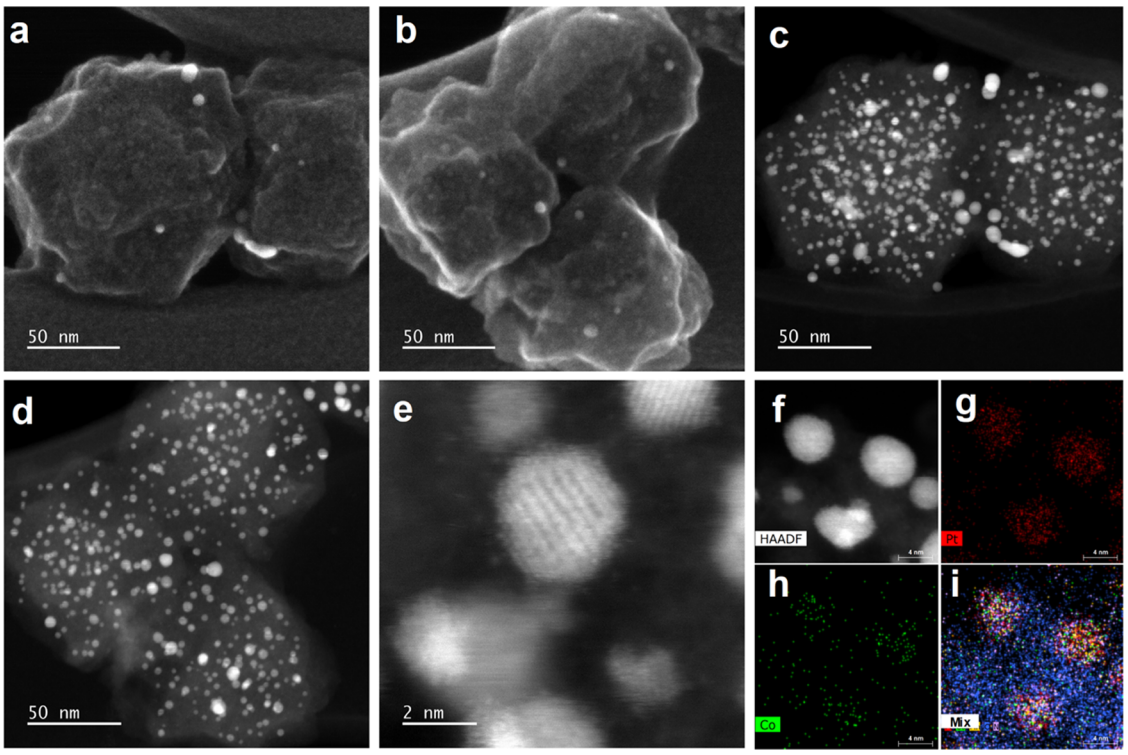

Figure 5. (a, b) Secondary electron (SE) images of aged Pt@Mn_{SA}-NC (a) and $L1_2$-Pt_3Co@Mn_{SA}-NC (b) after the AST. (c, d) Corresponding HAADF-STEM images of aged Pt@Mn_{SA}-NC (c) and $L1_2$-Pt_3Co@Mn_{SA}-NC (d). (e, f) HAADF-STEM images of aged $L1_2$-Pt_3Co@Mn_{SA}-NC. (g-i) STEM-EDS elemental distribution mapping of aged $L1_2$-Pt_3Co@Mn_{SA}-NC.

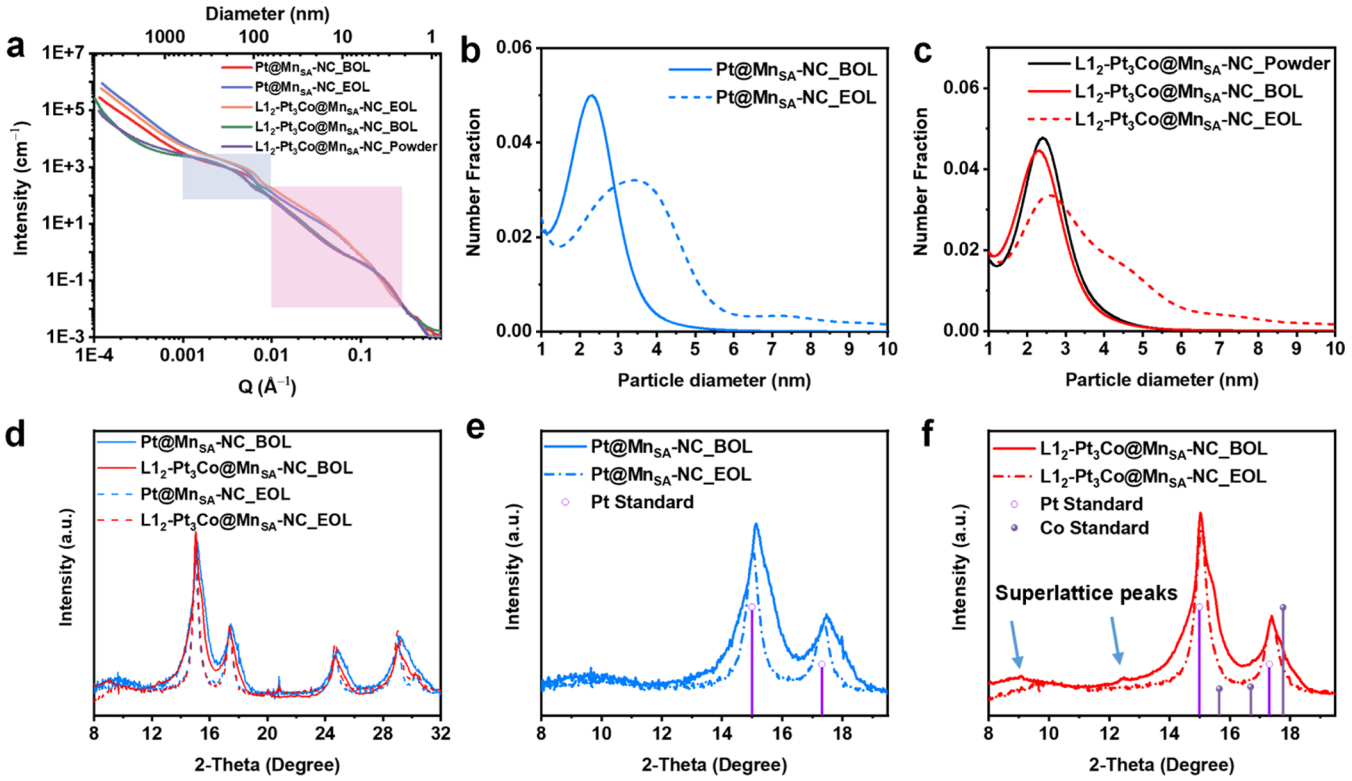

Figure 6. (a) Ultrasmall-angle X-ray scattering (USAXS) profiles. (b, c) MaxEnt particle size distribution for Pt@Mn_{SA}-NC (b) and $L1_2$-Pt_3Co@Mn_{SA}-NC (c) catalysts at BOL and EOL. (d) Wide-angle X-ray scattering (WAXS) curves for the Pt@Mn_{SA}-NC and PtCo@Mn_{SA}-NC catalysts before (BOL) and after (EOL) the AST. (e, f) WAXS region showing (111 and 200) reflections for the Pt@Mn_{SA}-NC (e) and PtCo@Mn_{SA}-NC (f) catalysts.

https://doi.org/10.1021/jacs.3c03345
J. Am. Chem. Soc. 2023, 145, 17643−17655

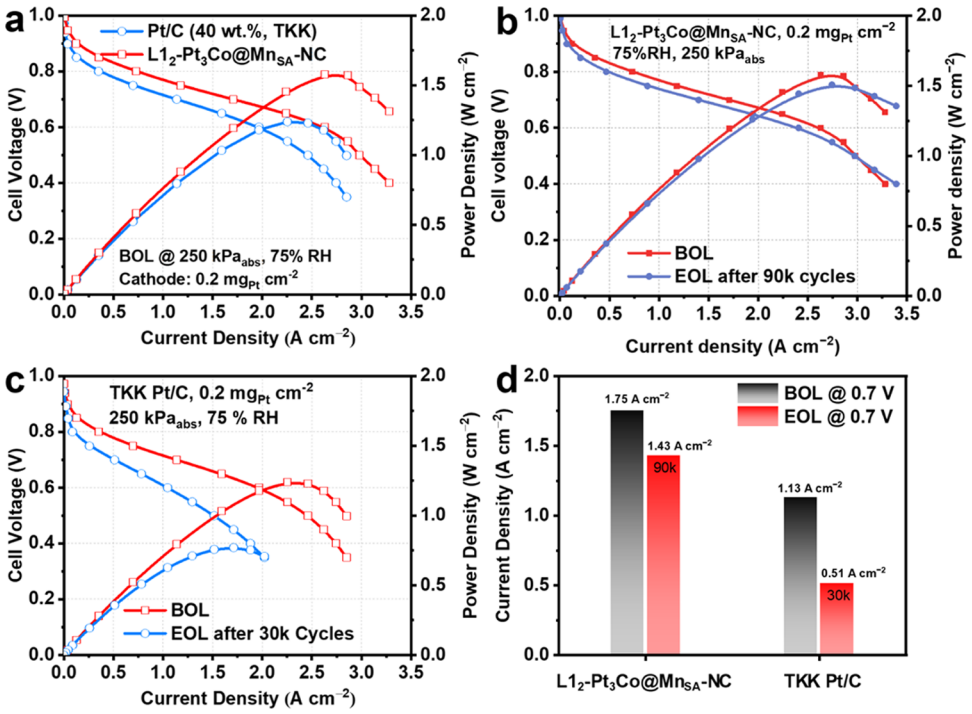

Figure 7. (a) BOL single-cell H_2/air performance of Pt/C and L1$_2$-Pt$_3$Co@Mn$_{SA}$-NC cathode in MEAs under HDV conditions (back pressure is 250 kPa$_{abs}$ and the Pt loading in the cathode is 0.2 mg$_{Pt}$ cm^{-2}). (b) MEA performance of L1$_2$-Pt$_3$Co@Mn$_{SA}$-NC cathode after 90,000 cycles under the HDV condition. (c) Fuel-cell performance of the 20% Pt/C catalyst after 30,000 cycles. (d) Current density at 0.7 V of L1$_2$-Pt$_3$Co@Mn$_{SA}$-NC and Pt/C before and after 90,000 cycles of the corresponding ASTs.

hydrophilicity of both cathodes was increased (Figures S22 and S23). The corresponding MA at 0.9 V and the current density at 0.7 V of the L1$_2$-Pt$_3$Co@Mn$_{SA}$-NC cathode declined to 0.45 A mg$_{Pt}^{-1}$ and 1.19 A cm^{-2}, respectively (Figure 4i). The MA at EOL is still higher than that at the DOE target (0.44 A mg$_{Pt}^{-1}$). The voltage loss (40 mV, 6%) at 0.8 A cm^{-2} was still larger than the challenging DOE target of 30 mV (Table S4).[12,31] The slightly inferior stability compared to RDE results is likely due to the contamination or damage of the ionomer caused by dissolved Co ions,[53,54] which is discussed in the following section.

2.5. Catalyst Degradation Mechanisms in an MEA. Cathode catalysts in the MEA after the AST were characterized with advanced electron microscopy and elemental analysis techniques. As shown in Figure 5a,b, the Mn$_{SA}$-NC support retained intact morphology, indicating its good electrochemical and mechanical stability. Statistical results indicate that the Pt-based NP sizes of both Pt@Mn$_{SA}$-NC and L1$_2$-Pt$_3$Co@Mn$_{SA}$-NC were increased slightly (Figures 5c,d and S25). In particular, the L1$_2$-Pt$_3$Co NPs increased to 4.0 ± 1.4 nm (Figure S26), slightly larger than the initial size (3.3 ± 1.1 nm). Yet, a large proportion of the NPs (85% for Pt and 72% for L1$_2$-Pt$_3$Co) still retained a size smaller than 4 nm rather than undergoing severe particle agglomeration often observed with commercial Pt/C catalysts (Figures S26 and S27).[55,56] This further highlights the advantages of the Mn$_{SA}$-NC support in preserving Pt-based NPs during AST cycling. According to atomic-resolution HAADF-STEM images, the ordered L1$_2$-Pt$_3$Co intermetallic structure was partially retained (Figure 5e). Meanwhile, Pt and Co elements are still apparent in the NPs (Figure 5f), but the atomic ratio of Pt to Co was increased from 73:27 to 93:7 due to Co dissolution (Table S5).

The size change of the Pt NPs within these MEAs after the AST was further investigated using small-angle X-ray scattering (SAXS). Figure 6a shows the SAXS scattered intensity ($I(q)$) versus the scattering vector (q) for the entire region. The marked regions in Figure 6a show scattering from Pt, L1$_2$-Pt$_3$Co NPs ($q \sim 0.01-0.3$ Å^{-1}), and Mn$_{SA}$-NC aggregates ($q \sim 0.001-0.01$ Å^{-1}) to large agglomerates ($q < 0.001$ Å^{-1}, likely carbon). Particle size distributions (PSDs) for Pt and PtCo NPs shown in Figures 6b and 6c, respectively, are obtained by fitting the scattering data in the q region between 0.01 and 0.3 Å^{-1} using the maximum entropy (MaxEnt) method (Table S6). The Pt@Mn$_{SA}$-NC and L1$_2$-Pt$_3$Co@Mn$_{SA}$-NC catalysts at BOL show mean particle diameters of 2.3 and 2.2 nm, respectively. After the AST, their mean particle diameters were slightly increased to 3.0 ± 1.1 and 3.0 ± 1.2 nm, respectively, consistent with HAADF-STEM analysis. The largely preserved particle size is likely ascribed to the strong chemical binding between the Mn$_{SA}$-NC support and Pt-based NPs and the physical hosting effect of the Mn$_{SA}$-NC support with a curved surface and porous architecture.

The crystal structures of the catalysts before and after the AST were also investigated using wide-angle X-ray scattering (WAXS). The WAXS profiles were acquired over a 2θ range from 5 to 35°, displaying peaks for the Pt(111), (200), (220), and (311) face-centered cubic (fcc) reflections (Figure 6d). Superlattice peaks around 12.5 and 19° can be observed in L1$_2$-Pt$_3$Co@Mn$_{SA}$-NC before the AST, verifying ordered intermetallic structures. The first two reflections (111 and 200) are presented in Figure 6e,6f, in which the reflections from Pt and Co are included as references. The WAXS patterns for the Pt@Mn$_{SA}$-NC and L1$_2$-Pt$_3$Co@Mn$_{SA}$-NC catalysts at BOL display broad and asymmetrical peaks due to the small grain sizes of Pt and L1$_2$-Pt$_3$Co NPs. After the AST,

https://doi.org/10.1021/jacs.3c03345
J. Am. Chem. Soc. 2023, 145, 17643−17655

the peaks of both samples become narrower and symmetrical, indicating an increase in the particle size. As for the $L1_2$-$Pt_3Co@Mn_{SA}$-NC catalyst, the peak positions decrease to lower 2θ, approaching pure Pt reference, and the superlattice peaks are barely identified due to Co dissolution, suggesting that the remaining ordering degree is less than 10%. The dissolved Co^{2+} ion may contaminate the ionomer or the membrane, causing loss of O_2 and proton transports and the observed MEA performance degradation.

Possible degradation mechanisms of the catalysts in MEAs are discussed here based on the changes in morphologies, structures, and chemical compositions of the catalysts after the AST. Due to the unique Mn_{SA}-NC support that can chemically or physically anchor the NPs against aggregation, many fine NPs are well preserved, contributing to the extraordinary stability of the $Pt@Mn_{SA}$-NC catalyst in MEAs. However, the inferior stability of $L1_2$-$Pt_3Co@Mn_{SA}$-NC to the $Pt@Mn_{SA}$-NC catalyst is due to the insufficient ordering degree of the intermetallic structures and the consequent Co dissolution. Innovative strategies to increase the ordering degree of PtCo catalysts are essential for continuously improving the long-term durability of PtCo-based catalysts.

2.6. MEA Performance and Stability under HDV Conditions. Considering the good initial activity and promising stability of $L1_2$-$Pt_3Co@Mn_{SA}$-NC catalyst under the LDV conditions (retaining 1.19 A cm^{-2} at 0.7 V after the AST), we further evaluated its MEA performance under HDV conditions (a higher Pt loading of 0.2 mg_{Pt} cm^{-2} and back pressure of 250 kPa_{abs}). A commercial Pt/C catalyst was used as a reference. Figure 7a shows the H_2−air MEA performance of the Pt/C and $L1_2$-$Pt_3Co@Mn_{SA}$-NC catalysts at RH of 75%. The $L1_2$-$Pt_3Co@Mn_{SA}$-NC MEA generated an impressive current density of 1.71 A cm^{-2} at 0.7 V and a high peak power density of 1.58 W cm^{-2}, significantly higher than those of the Pt/C MEA (1.13 A cm^{-2} and 1.24 W cm^{-2}). Meanwhile, the $L1_2$-$Pt_3Co@Mn_{SA}$-NC catalyst in the HDV MEA achieved an MA of 0.49 A mg_{Pt}^{-1} at 0.9 $V_{iR\text{-free}}$. Generally, the MA of PGM catalysts in MEAs is greatly dependent on catalyst loading, catalyst/ionomer interfaces, mass and charge transfer, and electrode structures (e.g., porosity). Therefore, the relatively low MA observed with $L1_2$-$Pt_3Co@Mn_{SA}$-NC in an HDV MEA is due to the high Pt loading, thicker electrode, higher oxygen/proton transport resistance, different ionomers (Aquivion D72-25BS for LDV vs. Nafion D520 for HDV), and reduced Pt utilization.[57,58]

We also systematically investigated the RH dependence of MEA performance because HDVs are desirable to operate at relatively low RHs. As shown in Figure S28, with decreasing RH, the peak power density of the $L1_2$-$Pt_3Co@Mn_{SA}$-NC MEA gradually increased from 1.49 (100% RH) to 1.66 W cm^{-2} (50% RH). The sensitive MEA performance to RH is likely attributed to the increased catalyst layer thickness due to a high Pt loading (0.20 mg_{Pt} cm^{-2}), which cannot efficiently remove the produced water. The doubled Pt loading in the cathode significantly improves stability (Figures 7b,d and S28). After the initial 30,000 cycles, the current density at 0.7 V only dropped to 1.52 A cm^{-2}. In contrast, the commercial Pt/C MEA suffered from a 55% loss at 0.7 V (Figure 7c,d).

After extensive 90,000 AST cycles, the MA only declined from 0.49 to 0.31 A mg_{Pt}^{-1}, a 37% loss (Table S7). Significantly, the $L1_2$-$Pt_3Co@Mn_{SA}$-NC MEA maintained a high current density of 1.43 A cm^{-2} at 0.7 V, corresponding to an 18% loss after the extended AST (Figure 7d and Table S7). It should be noted that a standard differential cell (Figure S29) with an active area of 5 cm^2 was designed for all MEA tests, which can fairly compare with the performance and durability reported in the recent literature.[12,59] Therefore, the remarkable activity and much-enhanced stability of the $L1_2$-$Pt_3Co@Mn_{SA}$-NC catalyst under HDV conditions are promising to meet the challenging DOE targets (1.07 Acm^{-2} at 0.7 V after a 25,000 h equivalent operation).

3. CONCLUSIONS

In summary, we theoretically and experimentally elucidate a strong coupling effect between single-metal site-rich carbon and Pt NPs. Among various single-metal-site-rich carbons, Mn_{SA}-NC presented a great potential to boost ORR activity and stability of Pt-based catalysts, likely due to its single-metal-site dopants (i.e., MnN_4) and unique morphologies (i.e., high surface areas, dominant micropore, reasonable graphitization degree, curved surface, and homogeneous polyhedron particles). In particular, integrating Mn_{SA}-NC and Pt yields strengthening interactions and weakening the E_{OH}. Consequently, well-dispersed Pt and ordered $L1_2$-Pt_3Co NPs on the Mn_{SA}-NC support are designed as cathode ORR catalysts.

The $Pt@Mn_{SA}$-NC catalyst in an LDV MEA delivered an MA of 0.63 A mg_{Pt}^{-1} (0.9 $V_{iR\text{-free}}$) and 1.05 A cm^{-2} (0.7 V, H_2−air fuel cell) with a Pt loading of 0.1 mg cm^{-2} and 150 kPa_{abs}. After 30,000 AST cycles, the loss in MA and current density at 0.7 V are insignificant, i.e., 22% and 9%, respectively. The remarkable activity and stability further verified the synergy derived from the Mn_{SA}-NC carbon support. Forming ordered $L1_2$-Pt_3Co intermetallics further enhances ORR activity. The resultant $L1_2$-$Pt_3Co@Mn_{SA}$-NC catalyst achieved MA values of 0.91 A mg_{Pt}^{-1} (0.9 $V_{iR\text{-free}}$) and 1.63 A cm^{-2} in an MEA under identical conditions. However, the compromised stability is likely due to insufficient ordering of the structure, causing Co dissolution.

Importantly, the $L1_2$-$Pt_3Co@Mn_{SA}$-NC catalyst exhibited promising performance and long-term durability under HDV conditions (high Pt loading: 0.2 mg_{Pt} cm^{-2} and high back pressure: 250 kPa_{abs}). The initial current density at 0.7 V was 1.75 A cm^{-2} and the catalyst only lost 37% of its BOL MA and 18% current density at 0.7 V after long-term 90,000 AST cycles, promising to meet the DOE targets for HDVs (>1.07 A cm^{-2} at 0.7 V after 25,000 h equivalent operations).

Electron microscopy and X-ray scattering studies indicate that the $Pt@Mn_{SA}$-NC and $L1_2$-$Pt_3Co@Mn_{SA}$-NC catalysts showed only mild particle coarsening after the AST, retaining an average particle size of 3.6 and 4.0 nm, respectively, likely due to the strong chemical coupling or physical confinement between the Mn_{SA}-NC support and PGM NPs. Hence, leveraging the knowledge in developing PGM-free M_{SA}−N−C catalysts as advanced carbon supports is an effective approach to designing synergistic low-PGM fuel-cell catalysts with enhanced performance and durability for newly emerging HDV applications. Beyond single-metal site-rich carbon, further exploring innovative carbon supports with dual-metal sites may provide additional benefits to strengthen PGM NPs and regulate their electronic structures for possible enhancements of intrinsic activity and stability.[60−62]

Notably, although the unique coupling effect could minimize the aggregation of Pt NPs under fuel-cell operating conditions and enhance intrinsic activity, the evitable Co dissolution still caused performance degradation, especially at a low Pt loading (0.1 mg_{Pt} cm^{-2}), due to the relatively low ordering structures

https://doi.org/10.1021/jacs.3c03345
J. Am. Chem. Soc. 2023, 145, 17643−17655

in the presenting PtCo alloy catalysts. Therefore, innovative strategies are in high demand to regulate PtCo intermetallic structures, aiming to mitigate Co dissolution and improve intrinsic stability.

■ ASSOCIATED CONTENT

Supporting Information

The Supporting Information is available free of charge at https://pubs.acs.org/doi/10.1021/jacs.3c03345.

HAADF-STEM, Raman, XRD, and electrochemical performance (PDF)

■ AUTHOR INFORMATION

Corresponding Authors

Jian Xie − *Department of Mechanical and Energy Engineering, Purdue School of Engineering and Technology, Indiana University-Purdue University Indianapolis, Indianapolis, Indiana 46202, United States;* orcid.org/0000-0002-9800-0206; Email: jianxie@iupui.edu

Deborah J. Myers − *Chemical Sciences and Engineering Division, Argonne National Laboratory, Lemont, Illinois 60439, United States;* orcid.org/0000-0001-9299-3916; Email: dmyers@anl.gov

Gang Wu − *Department of Chemical and Biological Engineering, University at Buffalo, The State University of New York, Buffalo, New York 14260, United States;* orcid.org/0000-0003-0885-6172; Email: gangwu@buffalo.edu

Authors

Yachao Zeng − *Department of Chemical and Biological Engineering, University at Buffalo, The State University of New York, Buffalo, New York 14260, United States*

Jiashun Liang − *Department of Chemical and Biological Engineering, University at Buffalo, The State University of New York, Buffalo, New York 14260, United States*

Chenzhao Li − *Department of Mechanical and Energy Engineering, Purdue School of Engineering and Technology, Indiana University-Purdue University Indianapolis, Indianapolis, Indiana 46202, United States; School of Mechanical Engineering, Purdue University, West Lafayette, Indiana 47907, United States;* orcid.org/0000-0002-6836-376X

Zhi Qiao − *Department of Chemical and Biological Engineering, University at Buffalo, The State University of New York, Buffalo, New York 14260, United States*

Boyang Li − *Department of Mechanical Engineering and Materials Science, University of Pittsburgh, Pittsburgh, Pennsylvania 15260, United States*

Sooyeon Hwang − *Center for Functional Nanomaterials, Brookhaven National Laboratory, Upton, New York 11973, United States;* orcid.org/0000-0001-5606-6728

Nancy N. Kariuki − *Chemical Sciences and Engineering Division, Argonne National Laboratory, Lemont, Illinois 60439, United States*

Chun-Wai Chang − *School of Chemical, Biological, and Environmental Engineering, Oregon State University, Corvallis, Oregon 97331, United States*

Maoyu Wang − *School of Chemical, Biological, and Environmental Engineering, Oregon State University, Corvallis, Oregon 97331, United States; X-ray Science Division, Argonne National Laboratory, Lemont, Illinois 60439, United States*

Mason Lyons − *School of Chemical, Biological, and Environmental Engineering, Oregon State University, Corvallis, Oregon 97331, United States*

Sungsik Lee − *X-ray Science Division, Argonne National Laboratory, Lemont, Illinois 60439, United States;* orcid.org/0000-0002-1425-9852

Zhenxing Feng − *School of Chemical, Biological, and Environmental Engineering, Oregon State University, Corvallis, Oregon 97331, United States;* orcid.org/0000-0001-7598-5076

Guofeng Wang − *Department of Mechanical Engineering and Materials Science, University of Pittsburgh, Pittsburgh, Pennsylvania 15260, United States;* orcid.org/0000-0001-8249-4101

David A. Cullen − *Center for Nanophase Materials Sciences, Oak Ridge National Laboratory, Oak Ridge, Tennessee 37831, United States;* orcid.org/0000-0002-2593-7866

Complete contact information is available at: https://pubs.acs.org/10.1021/jacs.3c03345

Author Contributions

¶Y.Z., J.L., and C.L. contributed equally. The manuscript was written through the contributions of all authors.

Notes

The authors declare no competing financial interest.

■ ACKNOWLEDGMENTS

This work was financially supported by the U.S. Department of Energy, Energy Efficiency and Renewable Energy Office, Hydrogen and Fuel-Cell Technologies Office (HFTO), the Million Mile Fuel-Cell Truck (M2FCT) consortium, and the SBIR Program from the Office of Science. Electron microscopy research was conducted at the Center for Functional Nanomaterials at the Brookhaven National Laboratory and the Center for Nanophase Materials Sciences at the Oak Ridge National Laboratory under Contract DE-SC0012704, DOE Office of Science User Facilities. The X-ray absorption (XSD, 12-BM) and scattering (XSD, 9-ID-C) experiments were performed at the Advanced Photon Source (APS), a DOE Office of Science User Facility operated for the DOE Office of Science by the Argonne National Laboratory under Contract No. DE-AC02-06CH11357. C.-W.C., M.W., M.L., and Z.F. acknowledge the financial support for this research provided by the National Science Foundation (NSF) (CBET-2016192 and CBET-1949870). B.L. and G.W. gratefully acknowledge the financial support for this research provided by the NSF (DMR 1905572). This work also used the computational resources provided by the University of Pittsburgh Center for Research Computing.

■ REFERENCES

(1) Staffell, I.; Scamman, D.; Abad, A. V.; Balcombe, P.; Dodds, P. E.; Ekins, P.; Shah, N.; Ward, K. R. The role of hydrogen and fuel cells in the global energy system. *Energy Environ. Sci.* **2019**, *12* (2), 463−491.

(2) Rudolf, T.; Schürmann, T.; Schwab, S.; Hohmann, S. Toward holistic energy management strategies for fuel cell hybrid electric vehicles in heavy-duty applications. *Proc. IEEE* **2021**, *109* (6), 1094−1114.

(3) Cullen, D. A.; Neyerlin, K. C.; Ahluwalia, R. K.; Mukundan, R.; More, K. L.; Borup, R. L.; Weber, A. Z.; Myers, D. J.; Kusoglu, A.

New roads and challenges for fuel cells in heavy-duty transportation. *Nat. Energy* **2021**, *6* (5), 462−474.
(4) Dirkes, S.; Leidig, J.; Fisch, P.; Pischinger, S. Prescriptive Lifetime Management for PEM fuel cell systems in transportation applications, Part II: On-board operando feature extraction, condition assessment and lifetime prediction. *Energy Convers. Manag.* **2023**, *283*, No. 116943.
(5) Kulkarni, A.; Siahrostami, S.; Patel, A.; Nørskov, J. K. Understanding Catalytic Activity Trends in the Oxygen Reduction Reaction. *Chem. Rev.* **2018**, *118* (5), 2302−2312.
(6) Wang, X. X.; Swihart, M. T.; Wu, G. Achievements, challenges and perspectives on cathode catalysts in proton exchange membrane fuel cells for transportation. *Nat. Catal.* **2019**, *2* (7), 578−589.
(7) Fan, J.; Chen, M.; Zhao, Z.; Zhang, Z.; Ye, S.; Xu, S.; Wang, H.; Li, H. Bridging the gap between highly active oxygen reduction reaction catalysts and effective catalyst layers for proton exchange membrane fuel cells. *Nat. Energy* **2021**, *6* (5), 475−486.
(8) Zhou, M.; Li, C.; Fang, J. Noble-metal based random alloy and intermetallic nanocrystals: Syntheses and applications. *Chem. Rev.* **2021**, *121* (2), 736−795.
(9) Zhao, Z.; Chen, C.; Liu, Z.; Huang, J.; Wu, M.; Liu, H.; Li, Y.; Huang, Y. Pt-based nanocrystal for electrocatalytic oxygen reduction. *Adv. Mater.* **2019**, *31* (31), No. 1808115.
(10) Liang, J.; Li, N.; Zhao, Z.; Ma, L.; Wang, X.; Li, S.; Liu, X.; Wang, T.; Du, Y.; Lu, G.; Han, J.; Huang, Y.; Su, D.; Li, Q. Tungsten-Doped L10-PtCo Ultrasmall Nanoparticles as a High-Performance Fuel Cell Cathode. *Angew. Chem., Int. Ed.* **2019**, *58* (43), 15471−15477.
(11) Yang, C.-L.; Wang, L.-N.; Yin, P.; Liu, J.; Chen, M.-X.; Yan, Q.-Q.; Wang, Z.-S.; Xu, S.-L.; Chu, S.-Q.; Cui, C.; Ju, H.; Zhu, J.; Lin, Y.; Shui, J.; Liang, H.-W. Sulfur-anchoring synthesis of platinum intermetallic nanoparticle catalysts for fuel cells. *Science* **2021**, *374* (6566), 459−464.
(12) Pan, Y.-T.; Li, D.; Sharma, S.; Wang, C.; Zachman, M. J.; Wegener, E. C.; Kropf, A. J.; Kim, Y. S.; Myers, D. J.; Peterson, A. A.; Cullen, D. A.; Spendelow, J. S. Ordered CoPt oxygen reduction catalyst with high performance and durability. *Chem. Catal.* **2022**, *2* (12), 3559−3572.
(13) Wang, X. X.; Hwang, S.; Pan, Y.-T.; Chen, K.; He, Y.; Karakalos, S.; Zhang, H.; Spendelow, J. S.; Su, D.; Wu, G. Ordered Pt3Co Intermetallic Nanoparticles Derived from Metal−Organic Frameworks for Oxygen Reduction. *Nano Lett.* **2018**, *18* (7), 4163−4171.
(14) Dai, Y.; Lu, P.; Cao, Z.; Campbell, C. T.; Xia, Y. The physical chemistry and materials science behind sinter-resistant catalysts. *Chem. Soc. Rev.* **2018**, *47* (12), 4314−4331.
(15) Li, J.; Sharma, S.; Liu, X.; Pan, Y.-T.; Spendelow, J. S.; Chi, M.; Jia, Y.; Zhang, P.; Cullen, D. A.; Xi, Z.; Lin, H.; Yin, Z.; Shen, B.; Muzzio, M.; Yu, C.; Kim, Y. S.; Peterson, A. A.; More, K. L.; Zhu, H.; Sun, S. Hard-Magnet $L1_0$-CoPt Nanoparticles Advance Fuel Cell Catalysis. *Joule* **2019**, *3* (1), 124−135.
(16) Dubau, L.; Maillard, F.; Chatenet, M.; André, J.; Rossinot, E. Nanoscale compositional changes and modification of the surface reactivity of Pt3Co/C nanoparticles during proton-exchange membrane fuel cell operation. *Electrochim. Acta* **2010**, *56* (2), 776−783.
(17) Durst, J.; Lamibrac, A.; Charlot, F.; Dillet, J.; Castanheira, L. F.; Maranzana, G.; Dubau, L.; Maillard, F.; Chatenet, M.; Lottin, O. Degradation heterogeneities induced by repetitive start/stop events in proton exchange membrane fuel cell: Inlet vs. outlet and channel vs. land. *Appl. Catal., B* **2013**, *138*−*139*, 416−426.
(18) Qiao, Z.; Wang, C.; Zeng, Y.; Spendelow, J. S.; Wu, G. Advanced Nanocarbons for Enhanced Performance and Durability of Platinum Catalysts in Proton Exchange Membrane Fuel Cells. *Small* **2021**, *17* (48), No. 2006805.
(19) Chung, D. Y.; Yoo, J. M.; Sung, Y. E. Highly durable and active Pt-based nanoscale design for fuel-cell oxygen-reduction electrocatalysts. *Adv. Mater.* **2018**, *30* (42), No. 1704123.
(20) Shao, Y.; Yin, G.; Gao, Y. Understanding and approaches for the durability issues of Pt-based catalysts for PEM fuel cell. *J. Power Sources* **2007**, *171* (2), 558−566.
(21) Mayrhofer, K. J.; Meier, J. C.; Ashton, S. J.; Wiberg, G. K.; Kraus, F.; Hanzlik, M.; Arenz, M. Fuel cell catalyst degradation on the nanoscale. *Electrochem. Commun.* **2008**, *10* (8), 1144−1147.
(22) Schulenburg, H.; Schwanitz, B.; Linse, N.; Scherer, G. n. G.; Wokaun, A.; Krbanjevic, J.; Grothausmann, R.; Manke, I. 3D imaging of catalyst support corrosion in polymer electrolyte fuel cells. *J. Phys. Chem. C* **2011**, *115* (29), 14236−14243.
(23) Samad, S.; Loh, K. S.; Wong, W. Y.; Lee, T. K.; Sunarso, J.; Chong, S. T.; Daud, W. R. W. Carbon and non-carbon support materials for platinum-based catalysts in fuel cells. *Int. J. Hydrogen Energy* **2018**, *43* (16), 7823−7854.
(24) Wu, G.; More, K. L.; Johnston, C. M.; Zelenay, P. High-performance electrocatalysts for oxygen reduction derived from polyaniline, iron, and cobalt. *Science* **2011**, *332* (6028), 443−447.
(25) Qiao, Z.; Zhang, H.; Karakalos, S.; Hwang, S.; Xue, J.; Chen, M.; Su, D.; Wu, G. 3D polymer hydrogel for high-performance atomic iron-rich catalysts for oxygen reduction in acidic media. *Appl. Catal., B* **2017**, *219*, 629−639.
(26) Zhang, H.; Hwang, S.; Wang, M.; Feng, Z.; Karakalos, S.; Luo, L.; Qiao, Z.; Xie, X.; Wang, C.; Su, D.; et al. Single atomic iron catalysts for oxygen reduction in acidic media: particle size control and thermal activation. *J. Am. Chem. Soc.* **2017**, *139* (40), 14143−14149.
(27) Li, J.; Chen, M.; Cullen, D. A.; Hwang, S.; Wang, M.; Li, B.; Liu, K.; Karakalos, S.; Lucero, M.; Zhang, H.; et al. Atomically dispersed manganese catalysts for oxygen reduction in proton-exchange membrane fuel cells. *Nat. Catal.* **2018**, *1* (12), 935−945.
(28) Shen, X. C.; Nagai, T.; Yang, F. P.; Zhou, L. Q.; Pan, Y. B.; Yao, L. B.; Wu, D. Z.; Liu, Y. S.; Feng, J.; Guo, J. H.; Jia, H. F.; Peng, Z. M. Dual-Site Cascade Oxygen Reduction Mechanism on SnOx/Pt-Cu-Ni for Promoting Reaction Kinetics. *J. Am. Chem. Soc.* **2019**, *141* (24), 9463−9467.
(29) Liu, S.; Li, C.; Zachman, M. J.; Zeng, Y.; Yu, H.; Li, B.; Wang, M.; Braaten, J.; Liu, J.; Meyer, H. M.; Lucero, M.; Kropf, A. J.; Alp, E. E.; Gong, Q.; Shi, Q.; Feng, Z.; Xu, H.; Wang, G.; Myers, D. J.; Xie, J.; Cullen, D. A.; Litster, S.; Wu, G. Atomically dispersed iron sites with a nitrogen−carbon coating as highly active and durable oxygen reduction catalysts for fuel cells. *Nat. Energy* **2022**, *7* (7), 652−663.
(30) Chen, M.; Li, X.; Yang, F.; Li, B.; Stracensky, T.; Karakalos, S.; Mukerjee, S.; Jia, Q.; Su, D.; Wang, G.; Wu, G.; Xu, H. Atomically Dispersed MnN4 Catalysts via Environmentally Benign Aqueous Synthesis for Oxygen Reduction: Mechanistic Understanding of Activity and Stability Improvements. *ACS Catal.* **2020**, *10* (18), 10523−10534.
(31) Qiao, Z.; Wang, C.; Li, C.; Zeng, Y.; Hwang, S.; Li, B.; Karakalos, S.; Park, J.; Kropf, A. J.; Wegener, E. C.; et al. Atomically dispersed single iron sites for promoting Pt and Pt 3 Co fuel cell catalysts: performance and durability improvements. *Energy Environ. Sci.* **2021**, *14* (9), 4948−4960.
(32) Chen, M.; Li, C.; Zhang, B.; Zeng, Y.; Karakalos, S.; Hwang, S.; Xie, J.; Wu, G. High-Platinum-Content Catalysts on Atomically Dispersed and Nitrogen Coordinated Single Manganese Site Carbons for Heavy-Duty Fuel Cells. *J. Electrochem. Soc.* **2022**, *169*, No. 034510.
(33) He, Y.; Wu, G. PGM-Free Oxygen-Reduction Catalyst Development for Proton-Exchange Membrane Fuel Cells: Challenges, Solutions, and Promises. *Acc. Mater. Res.* **2022**, *3* (2), 224−236.
(34) Chong, L.; Wen, J.; Kubal, J.; Sen, F. G.; Zou, J.; Greeley, J.; Chan, M.; Barkholtz, H.; Ding, W.; Liu, D.-J. Ultralow-loading platinum-cobalt fuel cell catalysts derived from imidazolate frameworks. *Science* **2018**, *362* (6420), 1276−1281.
(35) Ao, X.; Zhang, W.; Zhao, B.; Ding, Y.; Nam, G.; Soule, L.; Abdelhafiz, A.; Wang, C.; Liu, M. Atomically dispersed Fe−N−C decorated with Pt-alloy core−shell nanoparticles for improved activity and durability towards oxygen reduction. *Energy Environ. Sci.* **2020**, *13* (9), 3032−3040.

https://doi.org/10.1021/jacs.3c03345
J. Am. Chem. Soc. 2023, 145, 17643−17655

(36) Xiao, F.; Wang, Q.; Xu, G.-L.; Qin, X.; Hwang, I.; Sun, C.-J.; Liu, M.; Hua, W.; Wu, H.-w.; Zhu, S.; Li, J.-C.; Wang, J.-G.; Zhu, Y.; Wu, D.; Wei, Z.; Gu, M.; Amine, K.; Shao, M. Atomically dispersed Pt and Fe sites and Pt−Fe nanoparticles for durable proton exchange membrane fuel cells. *Nat. Catal.* **2022**, *5* (6), 503−512.
(37) Shao, Y.; Dodelet, J.-P.; Wu, G.; Zelenay, P. PGM-Free Cathode Catalysts for PEM Fuel Cells: A Mini-Review on Stability Challenges. *Adv. Mater.* **2019**, *31* (31), No. 1807615.
(38) He, Y.; Liu, S.; Priest, C.; Shi, Q.; Wu, G. Atomically dispersed metal−nitrogen−carbon catalysts for fuel cells: advances in catalyst design, electrode performance, and durability improvement. *Chem. Soc. Rev.* **2020**, *49* (11), 3484−3524.
(39) Tuinstra, F.; Koenig, J. L. Raman Spectrum of Graphite. *J. Chem. Phys.* **1970**, *53* (3), 1126−1130.
(40) Li, J.; Xi, Z.; Pan, Y.-T.; Spendelow, J. S.; Duchesne, P. N.; Su, D.; Li, Q.; Yu, C.; Yin, Z.; Shen, B.; Kim, Y. S.; Zhang, P.; Sun, S. Fe Stabilization by Intermetallic $L1_0$-FePt and Pt Catalysis Enhancement in $L1_0$-FePt/Pt Nanoparticles for Efficient Oxygen Reduction Reaction in Fuel Cells. *J. Am. Chem. Soc.* **2018**, *140* (8), 2926−2932.
(41) Motin, A. M.; Haunold, T.; Bukhtiyarov, A. V.; Bera, A.; Rameshan, C.; Rupprechter, G. Surface science approach to Pt/carbon model catalysts: XPS, STM and microreactor studies. *Appl. Surf. Sci.* **2018**, *440*, 680−687.
(42) Bergman, S. L.; Granestrand, J.; Tang, Y.; Paris, R. S.; Nilsson, M.; Tao, F. F.; Tang, C. H.; Pennycook, S. J.; Pettersson, L. J.; Bernasek, S. L. In-situ characterization by Near-Ambient Pressure XPS of the catalytically active phase of Pt/Al_2O_3 during NO and CO oxidation. *Appl. Catal., B* **2018**, *220*, 506−511.
(43) Ma, J.; Habrioux, A.; Luo, Y.; Ramos-Sanchez, G.; Calvillo, L.; Granozzi, G.; Balbuena, P. B.; Alonso-Vante, N. Electronic interaction between platinum nanoparticles and nitrogen-doped reduced graphene oxide: effect on the oxygen reduction reaction. *J. Mater. Chem. A* **2015**, *3* (22), 11891−11904.
(44) Hou, J.; Yang, M.; Ke, C.; Wei, G.; Priest, C.; Qiao, Z.; Wu, G.; Zhang, J. Platinum-group-metal catalysts for proton exchange membrane fuel cells: From catalyst design to electrode structure optimization. *EnergyChem* **2020**, *2* (1), No. 100023.
(45) Nørskov, J. K.; Rossmeisl, J.; Logadottir, A.; Lindqvist, L.; Kitchin, J. R.; Bligaard, T.; Jonsson, H. Origin of the overpotential for oxygen reduction at a fuel-cell cathode. *J. Phys. Chem. B* **2004**, *108* (46), 17886−17892.
(46) Wan, X.; Liu, X.; Li, Y.; Yu, R.; Zheng, L.; Yan, W.; Wang, H.; Xu, M.; Shui, J. Fe−N−C electrocatalyst with dense active sites and efficient mass transport for high-performance proton exchange membrane fuel cells. *Nat. Catal.* **2019**, *2* (3), 259−268.
(47) Uddin, A.; Dunsmore, L.; Zhang, H.; Hu, L.; Wu, G.; Litster, S. High Power Density Platinum Group Metal-free Cathodes for Polymer Electrolyte Fuel Cells. *ACS Appl. Mater. Interfaces* **2020**, *12* (2), 2216−2224.
(48) Zhao, X.; Yang, X.; Wang, M.; Hwang, S.; Karakalos, S.; Chen, M.; Qiao, Z.; Wang, L.; Liu, B.; Ma, Q.; Cullen, D. A.; Su, D.; Yang, H.; Zang, H.-Y.; Feng, Z.; Wu, G. Single-Iron Site Catalysts with Self-Assembled Dual-size Architecture and Hierarchical Porosity for Proton-Exchange Membrane Fuel Cells. *Appl. Catal., B* **2020**, *279*, No. 119400.
(49) Wang, M.; Feng, Z. Pitfalls in X-ray absorption spectroscopy analysis and interpretation: A practical guide for general users. *Curr. Opin. Electrochem.* **2021**, *30*, No. 100803.
(50) Wang, M.; Árnadóttir, L.; Xu, Z. J.; Feng, Z. In Situ X-ray Absorption Spectroscopy Studies of Nanoscale Electrocatalysts. *Nano-Micro Lett.* **2019**, *11* (1), No. 47.
(51) Luo, M.; Guo, S. Strain-controlled electrocatalysis on multimetallic nanomaterials. *Nat. Rev. Mater.* **2017**, *2* (11), 17059.
(52) Wang, Y.; Wang, D.; Li, Y. A fundamental comprehension and recent progress in advanced Pt-based ORR nanocatalysts. *SmartMat* **2021**, *2* (1), 56−75.
(53) Han, A.; Fu, C.; Yan, X.; Chen, J.; Cheng, X.; Ke, C.; Hou, J.; Shen, S.; Zhang, J. Effect of cobalt ion contamination on proton conduction of ultrathin Nafion film. *Int. J. Hydrogen Energy* **2020**, *45* (46), 25276−25285.
(54) Lee, C.; Wang, X.; Peng, J.-K.; Katzenberg, A.; Ahluwalia, R. K.; Kusoglu, A.; Komini Babu, S.; Spendelow, J. S.; Mukundan, R.; Borup, R. L. Toward a Comprehensive Understanding of Cation Effects in Proton Exchange Membrane Fuel Cells. *ACS Appl. Mater. Interfaces* **2022**, *14* (31), 35555−35568.
(55) Fan, L.; Zhao, J.; Luo, X.; Tu, Z. Comparison of the performance and degradation mechanism of PEMFC with Pt/C and Pt black catalyst. *Int. J. Hydrogen Energy* **2022**, *47* (8), 5418−5428.
(56) Kabir, S.; Myers, D. J.; Kariuki, N.; Park, J.; Wang, G.; Baker, A.; Macauley, N.; Mukundan, R.; More, K. L.; Neyerlin, K. C. Elucidating the Dynamic Nature of Fuel Cell Electrodes as a Function of Conditioning: An ex Situ Material Characterization and in Situ Electrochemical Diagnostic Study. *ACS Appl. Mater. Interfaces* **2019**, *11* (48), 45016−45030.
(57) Kriston, A.; Xie, T.; Ganesan, P.; Popov, B. N. Analysis of the Effect of Pt Loading on Mass and Specific Activity in PEM Fuel Cells. *J. Electrochem. Soc.* **2013**, *160* (4), F406.
(58) Nonoyama, N.; Okazaki, S.; Weber, A. Z.; Ikogi, Y.; Yoshida, T. Analysis of Oxygen-Transport Diffusion Resistance in Proton-Exchange-Membrane Fuel Cells. *J. Electrochem. Soc.* **2011**, *158* (4), B416.
(59) Gong, Q.; Zhang, H.; Yu, H.; Jeon, S.; Ren, Y.; Yang, Z.; Sun, C.-J.; Stach, E. A.; Foucher, A. C.; Yu, Y.; Smart, M.; Filippelli, G. M.; Cullen, D. A.; Liu, P.; Xie, J. Amino-tethering synthesis strategy toward highly accessible sub-3-nm L10-PtM catalysts for high-power fuel cells. *Matter* **2023**, *6* (3), 963−982.
(60) Yang, X.; Priest, C.; Hou, Y.; Wu, G. Atomically dispersed dual-metal-site PGM-free electrocatalysts for oxygen reduction reaction: Opportunities and challenges. *SusMat* **2022**, *2* (5), 569−590.
(61) Li, Y.; Shan, W.; Zachman, M. J.; Wang, M.; Hwang, S.; Tabassum, H.; Yang, J.; Yang, X.; Karakalos, S.; Feng, Z.; Wang, G.; Wu, G. Atomically Dispersed Dual-Metal Site Catalysts for Enhanced CO2 Reduction: Mechanistic Insight into Active Site Structures. *Angew. Chem., Int. Ed.* **2022**, *61* (28), No. e202205632.
(62) He, Y.; Yang, X.; Li, Y.; Liu, L.; Guo, S.; Shu, C.; Liu, F.; Liu, Y.; Tan, Q.; Wu, G. Atomically Dispersed Fe−Co Dual Metal Sites as Bifunctional Oxygen Electrocatalysts for Rechargeable and Flexible Zn−Air Batteries. *ACS Catal.* **2022**, *12* (2), 1216−1227.

https://doi.org/10.1021/jacs.3c03345
J. Am. Chem. Soc. 2023, 145, 17643−17655